



Anisotropic magnetic property of single crystals RV_6Sn_6 ($R = Y, Gd - Tm, Lu$)Jeonghun Lee  and Eundeok Mun 

Department of Physics, Simon Fraser University, 8888 University Drive, Burnaby, British Columbia, Canada V5A 1S6



(Received 6 June 2022; accepted 2 August 2022; published 16 August 2022)

RV_6Sn_6 ($R = Y, Gd - Tm, Lu$) single crystals are synthesized by the Sn-flux method and their physical properties are characterized by magnetization, resistivity, and specific heat measurements. Powder x-ray diffraction patterns of all samples can be well indexed with the hexagonal $HfFe_6Ge_6$ -type structure, where rare-earth atoms form hexagonal layers and vanadium atoms form kagome layers. At high temperatures, magnetic susceptibility measurements of moment-bearing rare-earth ions ($R = Gd - Tm$) follow Curie-Weiss behavior. Effective moments estimated from the polycrystalline average of magnetic susceptibility curves are consistent with the values for free R^{3+} ions. Strong magnetic anisotropy due to crystalline electric field effects is observed for moment-bearing rare-earth ions, except GdV_6Sn_6 . The easy magnetization direction is determined to be the c axis for $R = Tb - Ho$ and ab plane for $R = Er$ and Tm . The vanadium ions in RV_6Sn_6 possess no magnetic moment. The compounds for $R = Y$ and Lu exhibit typical characteristics of paramagnetic metals. At low temperatures, the magnetic ordering is confirmed from magnetization, specific heat, and resistivity: the highest $T_N = 4.9$ K for GdV_6Sn_6 and the lowest $T_N = 2.3$ K for HoV_6Sn_6 . No magnetic ordering is observed down to 1.8 K for $R = Er$ and Tm . A slight deviation of the magnetic ordering temperature from the de Gennes scaling suggests the dominant Ruderman-Kittel-Kasuya-Yosida exchange interaction between rare-earth moments in metallic RV_6Sn_6 compounds.

DOI: [10.1103/PhysRevMaterials.6.083401](https://doi.org/10.1103/PhysRevMaterials.6.083401)

I. INTRODUCTION

Intermetallic compounds with the chemical formula RT_6X_6 ($R =$ rare earth; $T = V, Cr, Mn, Fe, Co$; $X = Ge, Sn$) have shown complex magnetic and electronic properties that emerge from the interplay between localized $4f$ and itinerant $3d$ electrons [1–6]. The RT_6X_6 compounds crystallize into either the fully ordered $HfFe_6Ge_6$ -type or other disordered YCo_6Ge_6 -type or $SmMn_6Sn_6$ -type structure, depending on the size of the constituent $R, T,$ and X atoms [1,7–9]. In these crystal structures the rare-earth ions form hexagonal layers and the transition metal ions form kagome layers. When both R and T bear magnetic moments in their sublattices such as RMn_6Sn_6 , the compounds show temperature-dependent magnetic structures which are governed by the relative strength of $R-R, R-T,$ and $T-T$ exchange couplings [3,10]. In RMn_6Sn_6 , a strong antiferromagnetic coupling between rare-earth and Mn sublattices leads to a simultaneous ordering of both sublattices [2], where the compounds with $R = Gd - Ho$ show a collinear ferrimagnetic ordering above room temperatures and the compounds with $R = Er$ and Tm show an antiferromagnetic ordering of Mn sublattice at high temperatures followed by a ferrimagnetic ordering of R sublattice at low temperatures [11]. The magnetic structure of these compounds is highly dependent on crystalline electric field (CEF) [11]. It has been observed that when the transition metals bear no magnetic moment (e.g., $T = Cr$ and Co), a very low magnetic ordering temperature arises only from the rare-earth sublattice. For example, RCr_6Ge_6 compounds indicate the magnetic ordering below 15 K [5,12] and RCo_6X_6 ($X = Ge, Sn$) compounds

show the magnetic ordering below 3 K [13,14]. In particular, $GdCo_6Sn_6$ is a paramagnet down to 1.8 K [14].

In recent years, there have been considerable efforts to investigate topologically nontrivial states associated with the kagome lattice [15–17]. The RV_6Sn_6 compounds have gained attention due to their topologically nontrivial band structures [18–20], where RV_6Sn_6 can host 2D kagome surface states [21]. Measurements using angle-resolved photoemission spectroscopy (ARPES) on single crystals of RV_6Sn_6 ($R = Gd$ and Ho) and density functional theory calculations show characteristics of Dirac cones, saddle points, and flat bands, which arise from the vanadium kagome lattice [21]. It is also suggested that Dirac crossing at the K point gives rise to nonlinear Hall resistivity in GdV_6Sn_6 and YV_6Sn_6 [22].

Despite growing interest in electronic properties in the RV_6Sn_6 series, their magnetic properties have not yet been studied, except for $R = Gd$ and Y . Magnetization measurements on single crystals of RV_6Sn_6 ($R = Gd$ and Y) confirm that vanadium (V) ions possess no magnetic moments and Gd ions order antiferromagnetically below ~ 5 K [22,23]. Since the transition metal V is nonmagnetic, RV_6Sn_6 would provide an opportunity to study magnetic properties arising solely from the rare-earth triangular lattice. It has been reported that single crystals of RV_6Sn_6 grown by the flux method adopt the $HfFe_6Ge_6$ type for $R = Gd$ and Y [22], whereas polycrystalline samples of RV_6Sn_6 grown by the arc melt technique adopt the $SmMn_6Sn_6$ type for $R = Gd - Tm$ and Lu and the $HfFe_6Ge_6$ type for $R = Y$ [24]. In this report, we present the crystal structure and physical properties of RV_6Sn_6 ($R = Y, Gd - Tm, Lu$) single crystals grown by Sn flux.

II. EXPERIMENTS

Single crystals of RV_6Sn_6 ($R = Y, Gd - Tm, Lu$) were grown by Sn flux [25]. The constituent elements were cut into smaller pieces and placed in an alumina crucible in the ratio $R : V : Sn = 1 : 6 : 62$, and then sealed into an amorphous silica tube under partial argon atmosphere. The ampoule was heated up to 1225 °C over three hours, held there for five hours, and then slowly cooled down to 850 °C at a rate of 1.25 °C/hr. Single crystals were separated from the flux by centrifuging. The obtained single crystals have a platelike morphology with a clean hexagonal facet (ab plane) being the base of the plate as shown in the inset of Fig. 1(c). All grown single crystals have similar hexagonal morphology, but compounds with heavier rare-earth elements tend to form thicker single crystals. The average thickness of the obtained single crystals varies from ~ 0.2 mm (GdV_6Sn_6) to ~ 1 mm (LuV_6Sn_6).

To verify the crystal structure of the title compounds and their lattice parameters, powder x-ray diffraction (XRD) patterns of crushed single crystals were collected in a Rigaku MiniFlex diffractometer at room temperature and analyzed using a GSAS-II software [26]. The Si standard was used to minimize the instrumental error. The dc magnetization as a function of temperature from 1.8 to 300 K and magnetic fields up to 70 kOe were measured in a Quantum Design (QD) magnetic property measurement system (MPMS). Four-probe ac resistivity measurements were performed with $I \parallel ab$ from 300 K down to 1.8 K in a QD physical property measurement system (PPMS). Specific heat was measured by the relaxation technique down to 1.8 K in a QD PPMS.

III. RESULTS AND DISCUSSION

A. Crystal structure

The obtained and calculated powder XRD patterns for TbV_6Sn_6 , as a representative example in the series, are shown in Fig. 1(a). The observed peak positions are well indexed by the fully ordered $HfFe_6Ge_6$ -type structure ($P6/mmm$, No. 191). In earlier studies the two structural prototypes for RV_6Sn_6 compounds are reported [Fig. 1(b)]: single-crystalline samples (grown by Sn flux) for $R = Gd$ and Y [22] crystallize into the fully occupied $HfFe_6Ge_6$ type; polycrystalline samples (synthesized by arc melt) crystallize into the $HfFe_6Ge_6$ type for $R = Y$ and the $SmMn_6Sn_6$ type for $R = Gd - Tm$ [24]. The $SmMn_6Sn_6$ type is a disordered variant of the $HfFe_6Ge_6$ type. In the $SmMn_6Sn_6$ type, the fractional occupancy of additional R and Sn sites are reported to vary from 3% to 10%, depending on R [24]. In this study, the fully ordered $HfFe_6Ge_6$ -type structure is used to analyze the powder XRD patterns as it does not show any appreciable difference between the observed and calculated intensities, as shown in Fig. 1(a). The detection of subtle difference between the two structure types requires a much higher resolution diffractometer with rigorous Rietveld refinement.

The obtained lattice parameters c and a are shown in Figs. 2(a) and 2(b), respectively. Both a and c decrease with increasing R atomic number, following lanthanide contraction, implying that the valence state of the heavy rare-earth ions in RV_6Sn_6 compounds is trivalent. The lattice parameters

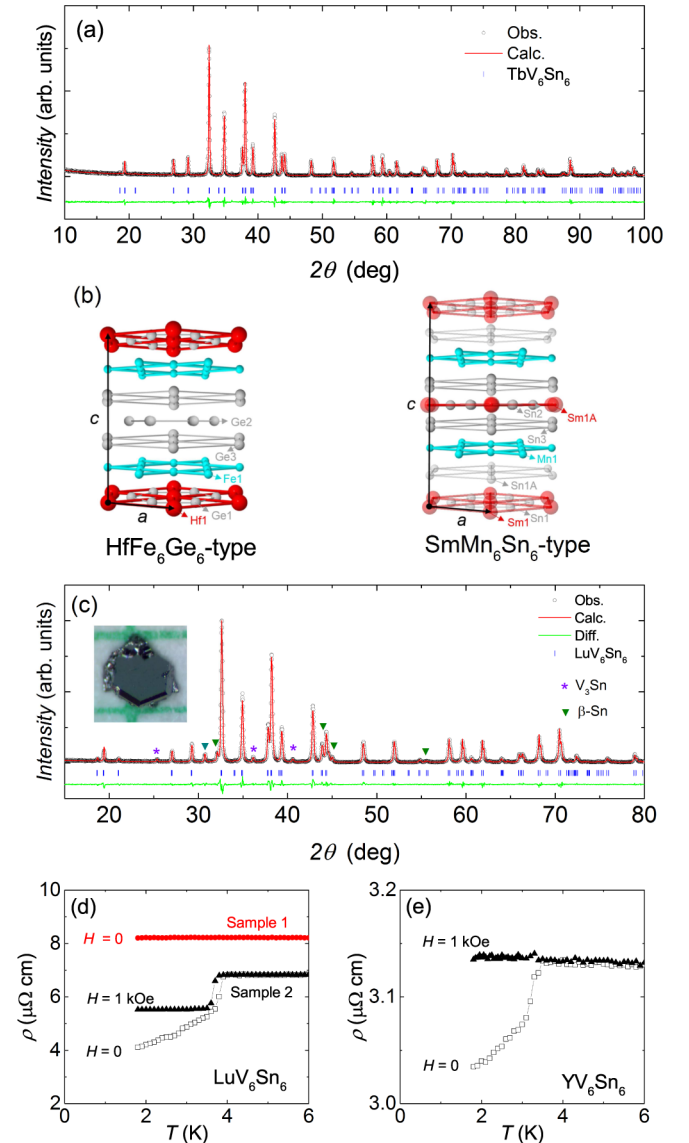


FIG. 1. (a) Powder XRD patterns of TbV_6Sn_6 . Red line is the calculated XRD patterns using $HfFe_6Ge_6$ -type structure. Green line represents the difference between the data and calculated patterns. (b) Schematics of $HfFe_6Ge_6$ -type and $SmMn_6Sn_6$ -type structure. To clearly show hexagonal rare-earth and kagome transition metal layers, c axis is not drawn to scale, where each layer is shifted upward. (c) Powder XRD patterns of LuV_6Sn_6 . Impurity phases of V_3Sn and β -Sn are marked by purple asterisk and green triangle symbols, respectively. Inset shows a photograph of LuV_6Sn_6 on mm grid. (d) Electrical resistivity of two LuV_6Sn_6 samples at $H = 0$ and 1 kOe. (e) Electrical resistivity of YV_6Sn_6 at $H = 0$ and 1 kOe.

obtained from earlier studies [22–24] are included in Fig. 2. The variations in lattice parameters are probably due to the different sample quality, refinement with different structure type, and instrumental error.

B. Impurity phase

The obtained powder XRD patterns and physical property measurements performed on this series show two minor

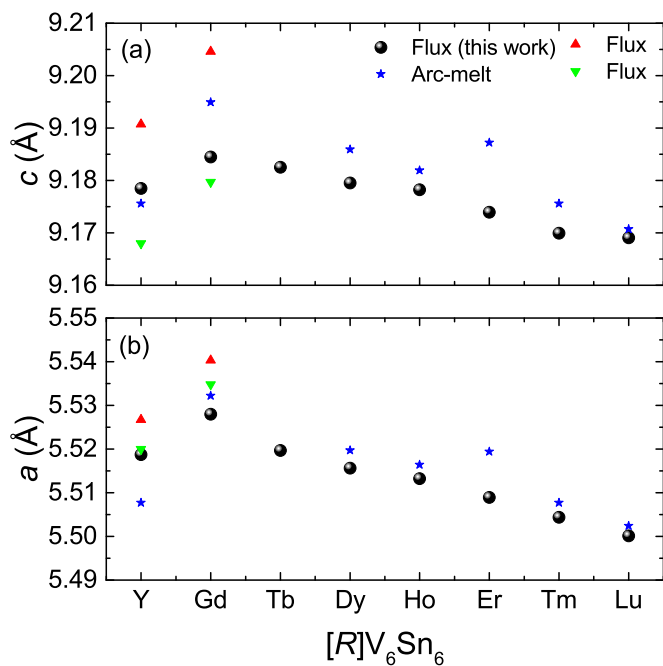


FIG. 2. (a) Lattice parameter c and (b) lattice parameter a as a function of rare-earth elements $[R]$ (black circles). Blue stars [24], red up-triangles [22], and green down-triangles [23] are taken from other reports.

impurity phases. As shown in Fig. 1(c), a traceable amount of V_3Sn and β -Sn phases is detected in LuV_6Sn_6 . Note that to demonstrate impurity phases detected in this family of materials, the XRD patterns, taken without cleaning sample surfaces, are presented in the figure. However, when small pieces of single crystals are carefully collected and surfaces of samples are polished or cleaned by diluted HCl acid, clean XRD patterns can be obtained as in the case for TbV_6Sn_6 . These two are the only impurity phases detected in the RV_6Sn_6 series and also consistent with impurities found in the previous report [24]. V_3Sn and β -Sn phases are known to have superconducting transitions at $T_c = 3.8$ K [27] and 3.7 K [28], respectively. The presence of these superconducting phases is clearly seen in electrical resistivity, $\rho(T)$, measurements. $\rho(T)$ curves on two different LuV_6Sn_6 samples are shown in Fig. 1(d). Samples 1 and 2 are two different pieces of single crystals grown from the same batch. $\rho(T)$ of the sample 1 indicates no resistivity drop below 4 K. $\rho(T)$ of the sample 2 shows the superconducting transition below 4 K at $H = 0$, which cannot be fully suppressed by applying magnetic field of 1 kOe. This is probably due to the superconducting V_3Sn phase. For the YV_6Sn_6 sample, its partial superconducting transition can be fully suppressed by a magnetic field of 1 kOe, as shown in Fig. 1(e). The superconducting transition in YV_6Sn_6 probably originates from β -Sn. It should be emphasized that superconducting transitions observed in resistivity measurements are not intrinsic to the ternary compound, as its resistivity does not go to zero below T_c . Thus, the superconducting transition below 4 K originates from impurity phases either on surfaces or embedded within the samples.

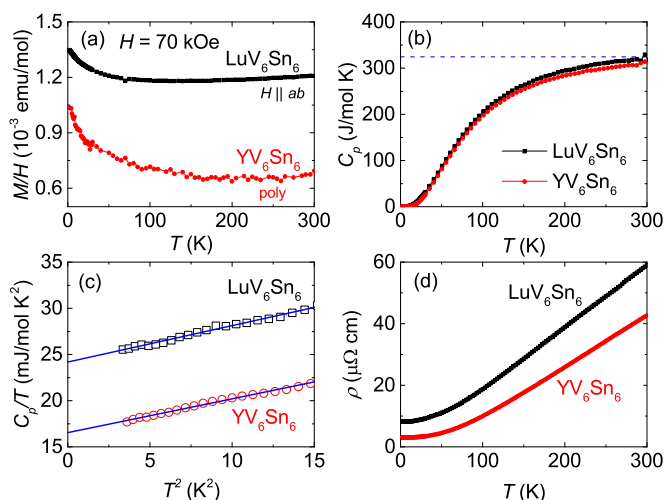


FIG. 3. Physical property measurements of LuV_6Sn_6 and YV_6Sn_6 . (a) M/H at $H = 70$ kOe. (b) Specific heat at $H = 0$. Horizontal line represents the Dulong-Petit limit. (c) C_p/T vs T^2 plot for LuV_6Sn_6 at $H = 20$ kOe and YV_6Sn_6 at $H = 30$ kOe. Solid lines represent fits to $C_p(T) = \gamma T + \beta T^3$. (d) Electrical resistivity at $H = 0$.

C. LuV_6Sn_6 and YV_6Sn_6

The temperature-dependent magnetic susceptibility, $\chi = M/H$, curves for $R = Lu$ and Y at $H = 70$ kOe are shown in Fig. 3(a). Due to the small size of single crystals, multiple pieces of YV_6Sn_6 were loaded into a gel capsule to measure magnetic susceptibility, which can be considered as a polycrystalline average. At high temperatures M/H curves of both samples are weakly dependent on temperature, while M/H curves at low temperatures exhibit an upturn probably due to paramagnetic impurities. The absolute value of magnetic susceptibility of both compounds is a bit larger than that of typical Y- and Lu-based intermetallic compounds [29–31]. For YV_6Sn_6 the absolute value of M/H at 300 K has a similar order of magnitude to previously reported values ($\sim 10^{-3}$ emu/mol) [22,23]. Thus, the enhanced magnetic susceptibility seems to be the generic feature in nonmagnetic RV_6Sn_6 compounds. From the magnetization measurements we infer that the V ions in these compounds do not carry magnetic moment. Typically, a magnetic moment on V is observed in vanadium complexes such as insulating spinel ZnV_2O_4 (V^{3+} , $S = 1$) [32] and triangular lattice antiferromagnet VCl_2 (V^{2+} , $S = 3/2$) [33]. The absence of the magnetic moment on V ions in RV_6Sn_6 implies quenching of the spin magnetic moment [34], where Sn atoms may have contributed to quenching of the spin moment on vanadium by forming metallic or covalent bonds, as evidenced by short V-Sn distances [24].

The temperature-dependent specific heat, $C_p(T)$, curves of LuV_6Sn_6 and YV_6Sn_6 are shown in Fig. 3(b). At high temperatures the $C_p(T)$ curves of both compounds are almost identical and approach the Dulong-Petit limit at 300 K. At low temperatures, $C_p(T)$ can be described by considering electronic and phonon contributions: $C_p(T) = \gamma T + \beta T^3$. Figure 3(c) shows plots of C_p/T vs T^2 for $R = Lu$ at $H = 20$ kOe and $R = Y$ at 30 kOe. Due to the superconducting transition below 4 K the specific heat data under magnetic field

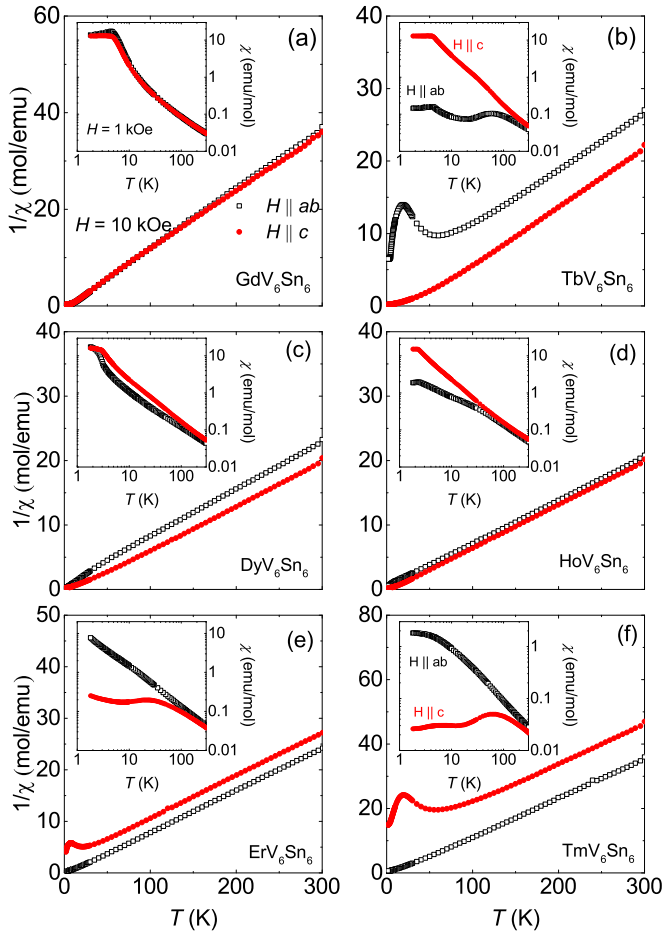


FIG. 4. Inverse magnetic susceptibility curves of $RV_6\text{Sn}_6$ ($R = \text{Gd} - \text{Tm}$) at $H = 10$ kOe for $H \parallel ab$ (open squares) and $H \parallel c$ (closed circles). Insets show M/H curves at $H = 1$ kOe.

are used to estimate the electronic specific heat coefficient (γ) and Debye temperature (θ_D). The obtained γ values are ~ 24 mJ/mole K^2 for $R = \text{Lu}$ and ~ 17 mJ/mole K^2 for $R = \text{Y}$. The estimated θ_D from β is ~ 400 K for both compounds. Note that a rather high γ value (~ 67 mJ/mole K^2), obtained by fitting the C/T vs T^2 curve from 200 to 600 K^2 , has been reported for the YV_6Sn_6 sample [23]. The $\rho(T)$ curves for both $R = \text{Lu}$ and Y are shown in Fig. 3(d). The resistivity curves decrease monotonically as temperature is lowered down to 1.8 K, following a typical metallic behavior.

TABLE I. A summary of magnetic properties of $RV_6\text{Sn}_6$ ($R = \text{Gd} - \text{Tm}$): magnetic ordering temperatures T_N^χ determined from $d\chi T/dT$ at $H = 1$ kOe, T_N^ρ determined from $d\rho/dT$ at $H = 0$, $T_N^{C_m}$ determined from the maximum in C_m ; easy magnetization direction; Weiss temperatures θ_p^{ab} , θ_p^c , and θ_p^{poly} ; effective moment μ_{eff} (theoretical value for free R^{3+} ion); and CEF parameter B_2^0 .

R	T_N^χ (K)	T_N^ρ (K)	$T_N^{C_m}$ (K)	Easy direction	θ_p^{ab} (K)	θ_p^c (K)	θ_p^{poly} (K)	μ_{eff} (μ_B/R^{3+})	B_2^0 (K)
Gd	4.8	5.0	4.9		0.9	-2.5	-0.2	8.1 (7.9)	0.2
Tb	4.3	4.2	4.2	c axis	-38.3	32.3	-14.3	10.0 (9.7)	-1.4
Dy	2.9	2.9	3.0	c axis	-13.4	17.0	-3.5	10.5 (10.7)	-0.4
Ho	2.3	2.3	2.4	c axis	-4.5	4.5	-1.5	10.9 (10.6)	-0.1
Er				ab plane	3.3	-29.9	-7.8	9.9 (9.6)	0.4
Tm				ab plane	10.3	-71.2	-17.2	8.1 (7.6)	1.7

D. Physical properties of $RV_6\text{Sn}_6$ ($R = \text{Gd} - \text{Tm}$)

The magnetic susceptibility of all moment-bearing members in $RV_6\text{Sn}_6$ follows the Curie-Weiss, $\chi(T) = C/(T - \theta_p)$, behavior at high temperatures. The inverse magnetic susceptibility, $1/\chi = H/M$, curves of $RV_6\text{Sn}_6$ are plotted in Fig. 4 for both $H \parallel ab$ and $H \parallel c$ at $H = 10$ kOe. A polycrystalline average is estimated by $\chi_{\text{poly}} = \frac{2}{3}\chi_{ab} + \frac{1}{3}\chi_c$. Effective moments, μ_{eff} , and Weiss temperatures, θ_p , are obtained by fitting $1/\chi$ curves above 150 K to the Curie-Weiss law. The effective moments of $RV_6\text{Sn}_6$ estimated from the polycrystalline average are close to that of free R^{3+} -ion values, as summarized in Table I, implying a 3+ valence state of the rare-earth ions ($R = \text{Gd} - \text{Tm}$) and no magnetic moment on V ions. Thus, magnetic properties of $RV_6\text{Sn}_6$ can be explained by considering 4f moments of rare-earth ions. The θ_p^{poly} values obtained from the polycrystalline average are negative for all rare-earths ions, indicating antiferromagnetic exchange interactions between rare-earth moments. For GdV_6Sn_6 , $\mu_{\text{eff}} = 8.1 \mu_B$ and $\theta_p = -0.2$ K, which is consistent with that of previous polycrystalline study [22]. However, θ_p of earlier single-crystal study is positive (~ 7.6 K) [23], which is somewhat larger than our result and another report [22]. This discrepancy may be related to different growth conditions.

The M/H curves of $RV_6\text{Sn}_6$, measured at $H = 1$ kOe for both $H \parallel ab$ and $H \parallel c$, are shown in the insets of Fig. 4. The M/H curves for $R = \text{Gd} - \text{Ho}$ show slope changes below 5 K as a signature of the antiferromagnetic ordering. The magnetic ordering temperature determined from $d\chi T/dT$ is $T_N = 4.8, 4.3, 2.9,$ and 2.3 K for $R = \text{Gd}, \text{Tb}, \text{Dy},$ and Ho , respectively. The magnetic ordering is not detected down to 1.8 K for $R = \text{Er}$ and Tm .

The magnetization isotherm, $M(H)$, at $T = 2$ K in this series clearly shows a magnetic anisotropy between $H \parallel ab$ and $H \parallel c$, as shown in Fig. 5. Magnetization measurements indicate no detectable hysteresis for all $RV_6\text{Sn}_6$. The easy magnetization direction is along the c axis for $R = \text{Tb}, \text{Dy},$ and Ho and ab plane for $R = \text{Er}$ and Tm . As expected, $M(H)$ of GdV_6Sn_6 indicates no anisotropy at high magnetic fields, but $M(H)$ for $H \parallel c$ is slightly smaller than that for $H \parallel ab$, as displayed in the inset of Fig. 5(a). The saturated magnetization values of GdV_6Sn_6 and TbV_6Sn_6 at 70 kOe are close to the theoretical values of free Gd ($7 \mu_B/\text{Gd}$) and Tb ($9 \mu_B/\text{Tb}$) ions. $M(H)$ of GdV_6Sn_6 is similar to ones observed in previous reports [22,23]. The saturated magnetization values for $R = \text{Dy} - \text{Tm}$ at 70 kOe are somewhat smaller than their

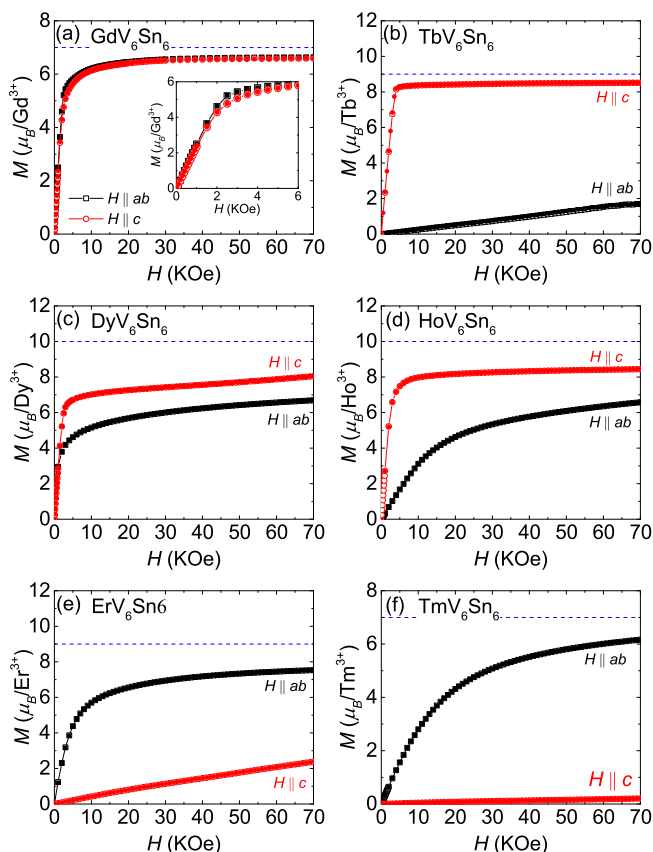


FIG. 5. Magnetization isotherms of RV_6Sn_6 ($R = \text{Gd} - \text{Tm}$) at $T = 2 \text{ K}$ for $H \parallel ab$ (squares) and $H \parallel c$ (circles). Open and closed symbols are data taken while increasing and decreasing magnetic fields, respectively. Horizontal dotted lines indicate the saturated magnetization values (gJ) for free R^{3+} ions. Inset in (a) shows an expanded plot between 0 and 6 kOe.

theoretical gJ values. The observed large magnetic anisotropy implies the presence of the strong CEF acting on $4f$ moments.

Figures 6(a)–6(f) present the $\rho(T)$ curves of RV_6Sn_6 . Note that due to the superconducting impurity phase $\rho(T)$ curves at $H = 1 \text{ kOe}$ for $R = \text{Gd}$, Tb , and Tm are plotted. At high temperatures, $\rho(T)$ follows typical metallic behavior with resistivity values ranging 10 - 100 $\mu\Omega \text{ cm}$ at 300 K. At low temperatures, $\rho(T)$ curves for $R = \text{Gd} - \text{Ho}$ show a sharp drop at T_N due to the loss of spin disorder scattering, indicated by arrows in the insets of Figs. 6(a)–6(d). $\rho(T)$ of GdV_6Sn_6 and YV_6Sn_6 is similar to that of previous reports [22,23].

Figure 7(a) shows the $C_p(T)$ curves for $R = \text{Gd} - \text{Tm}$ and Lu . The specific heat of all RV_6Sn_6 compounds reaches the value close to the Dulong-Petit limit at 300 K. At low temperatures, specific heat measurements for $R = \text{Gd} - \text{Ho}$ show λ -like peaks (insets) as signatures of magnetic ordering, which are better seen in the magnetic part of specific heat (C_m). The magnetic ordering temperatures, determined from the peak positions, for $R = \text{Gd}$, Tb , Dy , and Ho are $T_N = 4.9$, 4.2, 3.0, and 2.4 K, respectively, which are consistent with magnetic susceptibility and resistivity measurements. For $R = \text{Er}$ and Tm , no peak in $C_p(T)$ is observed down to 1.8 K. The low-temperature C_m curves for $R = \text{Gd} - \text{Tm}$ are obtained by subtracting the specific heat of LuV_6Sn_6 and plotted in

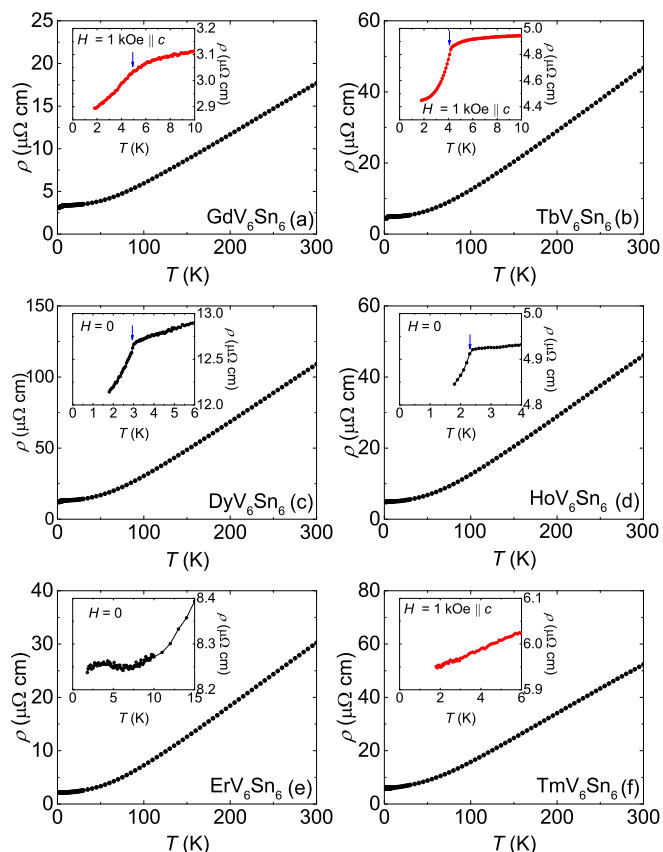


FIG. 6. Electrical resistivity, $\rho(T)$, curves of RV_6Sn_6 ($R = \text{Gd} - \text{Tm}$). Insets show $\rho(T)$ at low temperatures, where vertical arrows indicate the magnetic ordering temperatures. For $R = \text{Gd}$, Tb , and Tm , $\rho(T)$ at $H = 1 \text{ kOe}$ is presented.

Figs. 7(b) and 7(c). In addition to the sharp peaks at T_N , C_m curves show broad maxima at higher temperatures. These maxima correspond to the Schottky contributions, as the R^{3+} ions ($R = \text{Tb} - \text{Tm}$) are influenced by the CEF. It has to be noted that C_m of GdV_6Sn_6 shows an unusual Schottky-like anomaly (a broad maximum centered around 50 K), despite CEF splitting not being expected in Gd-based compounds. This anomaly may be due to the subtraction error.

The observed magnetic ordering temperatures for RV_6Sn_6 are plotted in Fig. 8 as a function of de Gennes factor. Unlike $R\text{Fe}_6\text{Ge}_6$ [6] and $R\text{Mn}_6\text{X}_6$ ($X = \text{Ge}$ and Sn) [2,4] which have magnetic ordering temperatures above the room temperature, RV_6Sn_6 compounds indicate the magnetic ordering at much lower temperatures. When the transition metals possess no magnetic moments in this family of materials such as $R\text{Co}_6\text{X}_6$ ($X = \text{Ge}$ and Sn) [14] and $R\text{Cr}_6\text{X}_6$ [5], a relatively low magnetic ordering temperature has been detected. Since the V ions possess no magnetic moments, the observed magnetic ordering is solely based on $4f$ moments, and thus a very low magnetic ordering temperature is seen.

When rare-earth ions are the only source of magnetism in an intermetallic compound, the magnetic ordering can be explained by indirect Ruderman-Kittel-Kasuya-Yosida (RKKY) exchange interaction. In the molecular field approximation, the ordering temperature is proportional to de Gennes factor $(g_J - 1)^2 J(J + 1)$ and can be defined as

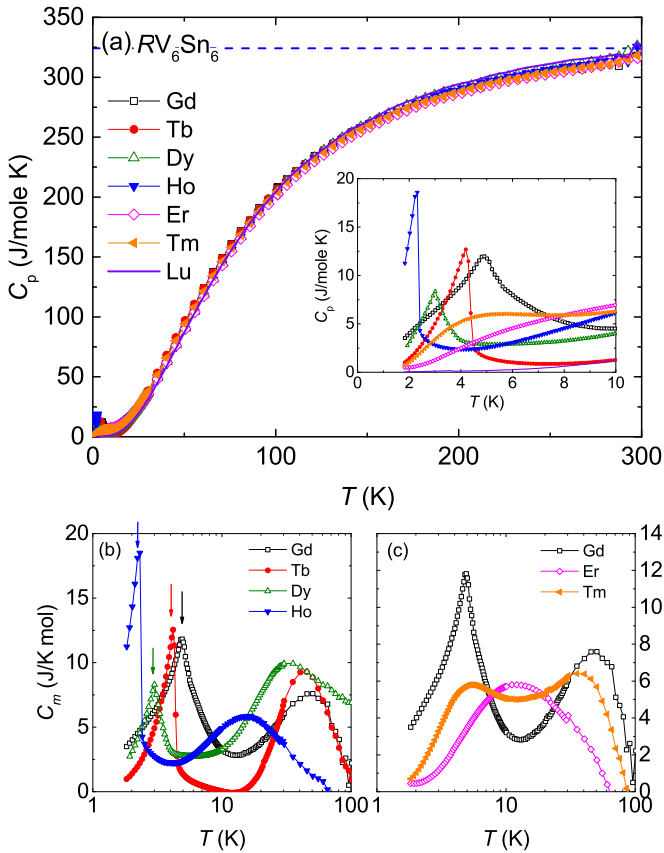


FIG. 7. (a) Specific heat C_p curves of RV_6Sn_6 ($R = Gd - Tm$ and Lu). Inset shows C_p below 10 K. (b) Magnetic part of the specific heat C_m for $R = Gd - Ho$. Vertical arrows indicate the magnetic ordering temperatures. (c) C_m for $R = Gd, Er$, and Tm .

$T_N = \frac{2}{3}\mathcal{J}(g_J - 1)^2J(J + 1)$, where \mathcal{J} is the exchange parameter, g is the Landé g factor, and J is the total angular momentum quantum number of the Hund's rule ground state of R^{3+} ions [35,36]. For the compounds with heavy rare-earth ions, T_N should decrease monotonically as R traverses from Gd to Yb . The ordering temperatures in many rare-earth-based intermetallic compounds follow this scaling [37–40]. However, when there are strong CEF effects, a deviation from the linear de Gennes scaling has been observed for $R = Tb - Yb$ [36,41,42]. As shown in Fig. 8, the magnetic ordering temperature of RV_6Sn_6 indicates a slight deviation from the de Gennes scaling, expected to be due to the CEF effects. The observed anisotropic magnetic susceptibility and magnetization isotherm and broad maxima in specific heat clearly reflect the CEF effects on RV_6Sn_6 compounds. In addition, there has been shown a switch of easy magnetization direction from the c axis for $R = Tb, Dy$, and Ho to ab plane for $R = Er$ and Tm in many tetragonal and hexagonal rare-earth-based intermetallic compounds [30,31,36]. Typically, due to the change in sign of leading crystal field parameter, the switch of easy magnetization direction occurs between Ho and Er . Based on the point charge model, the leading crystal field parameter B_2^0 in hexagonal symmetry can be obtained by $B_2^0 = \frac{10(\theta_p^{ab} - \theta_p^c)}{3(2J-1)(2J+3)}$ [43,44]. The estimated B_2^0 values from the magnetic susceptibility results are summarized in Table I. In RV_6Sn_6 , the B_2^0 changes a

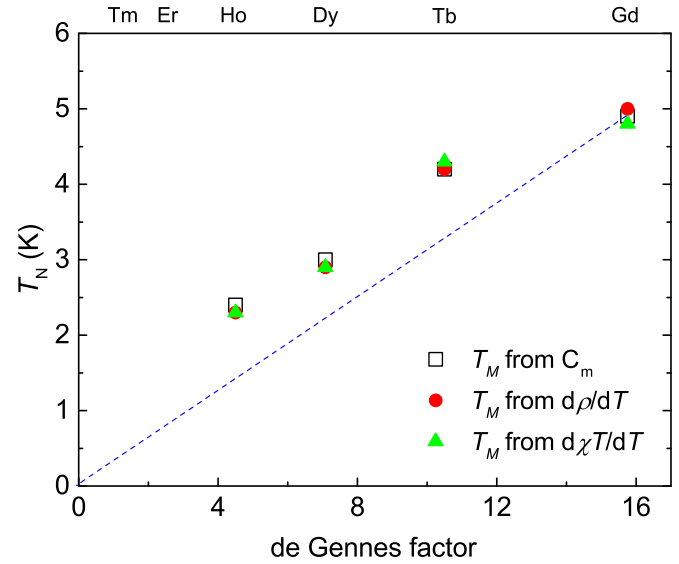


FIG. 8. Magnetic ordering temperature, T_N , as a function of de Gennes factor. The blue dashed line represents expected ordering temperatures for $R = Tb - Tm$ without CEF.

sign between Ho and Er , suggesting that the detected magnetic anisotropy is mainly associated with CEF. When the strong CEF exchange interaction is present, the magnetic ordering temperature depends on B_2^0 and the large value of B_2^0 gives rise to enhance the magnetic ordering temperature, which breaks the simple de Gennes picture [36]. In RV_6Sn_6 , although T_N for $Tb - Ho$ is enhanced, the maximum ordering temperature occurs in GdV_6Sn_6 and T_N still follows the monotonic decrease from Gd to Ho . This implies that CEF interaction to enhance T_N for $R = Tb - Ho$ is not large enough to exceed T_N for $R = Gd$ [36,45]. The B_2^0 value of TbV_6Sn_6 is greatest among c axis ordering RV_6Sn_6 compounds; however $B_2^0 \sim -1.4$ K is much smaller than that of other rare-earth-based compounds showing the highest ordering temperature for $R = Tb$ [36,45].

Although the estimated B_2^0 value for $R = Er$ and Tm is comparable to that for $R = Tb$ and Dy , no magnetic ordering is observed down to 1.8 K in these two compounds. This may be related to the geometric frustration in a triangular motif. In the present theoretical consensus the ground state of a two-dimensional triangular lattice is stabilized with a noncollinear 120° spin structure with a reduced sublattice magnetization [46–50]. However, the role of in-plane anisotropy and interplanar coupling must be included, which is relevant to spin-orbit-coupled $4f$ electron materials [51–55]. It would be interesting to investigate whether the triangular lattice geometry formed by rare-earth ions in RCO_6X_6 and RCr_6X_6 plays an important role. For $R = Er$ and Tm , experiments much below 1.8 K are in need to elucidate the existence of geometric frustration with easy-plane anisotropy.

The magnetic entropy, S_m , curves of RV_6Sn_6 are shown Fig. 9, where S_m is estimated by integrating C_m/T . Below 1.8 K, the missing entropy is estimated by assuming $C = 0$ at $T = 0$ K. S_m provides insight into the underlying CEF ground state of magnetic RV_6Sn_6 . At T_N , S_m of TbV_6Sn_6 reaches a value close to $R \ln(2)$, suggesting a possible pseudodoublet magnetic ground state (non-Kramers doublet, a singlet ground

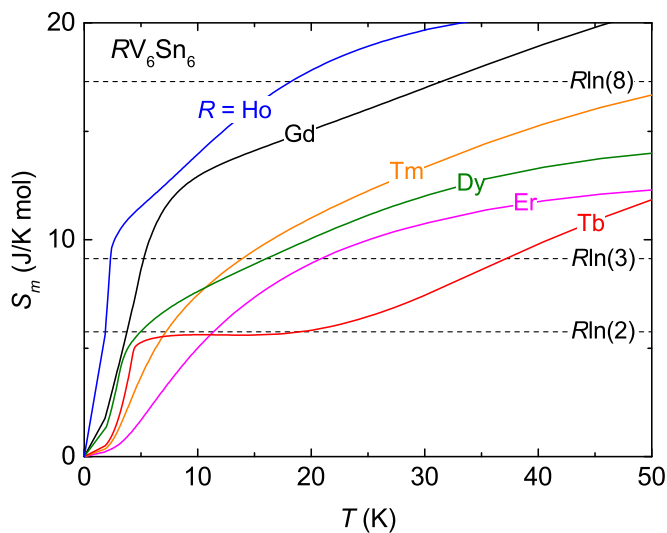


FIG. 9. Magnetic entropy, S_m , curves of RV_6Sn_6 ($R = Gd - Tm$).

state with a singlet excited state). For DyV_6Sn_6 , the value of S_m at T_N suggests a Kramers doublet ground state. For HoV_6Sn_6 , S_m at T_N reaches a value slightly above $R \ln(3)$, suggesting a possible triplet or pseudotriplet ground state (a singlet ground state with either a doublet excited state or two more singlet excited states, all with close energies). Note that the ground state entropy must be properly confirmed by specific heat measurements below 1.8 K. Interestingly, only $\sim 50\%$ of the $R \ln(8)$ magnetic entropy for GdV_6Sn_6 is recovered at T_N . In general, Gd^{3+} ions in intermetallic compounds are at $L = 0$ (S state); no CEF effect is expected. Therefore, the full $R \ln(8)$ magnetic entropy is expected to be recovered at the ordering temperature. However, for GdV_6Sn_6 the full $R \ln(8)$ entropy is recovered at ~ 30 K which is significantly higher than $T_N = 4.9$ K. Obviously the entropy is overestimated at high temperatures, where the entropy continues to increase beyond $R \ln(8)$ above 30 K, suggesting a subtraction error in the estimate of C_m . Since the obtained effective moment and saturation moment for GdV_6Sn_6 are close to the theoretical Gd^{3+} ion values, C_m is purely based on Gd magnetic contributions. When it is assumed that GdV_6Sn_6 has no additional magnetic transitions below 1.8 K, the reduced entropy at T_N cannot be simply related to the subtraction error. The reduced entropy may raise the possibility of a mixed magnetic structure, where both magnetic and nonmagnetic sites coexist on an equivalent crystallographic site. This kind of magnetic structure has been evident in geometrically frustrated metallic systems [56–58]. It has also been shown

theoretically and experimentally that the RKKY interaction in two-dimensional hexagonal lattice gives rise to complex spin structures and potentially hosts a skyrmion phase in conjunction with geometrical frustration [59–61]. A recent study on GdV_6Sn_6 has suggested that Gd ions form noncollinear spin structure below the magnetic ordering temperature [23].

Peculiar electronic states have been observed in Fe_3Sn_2 [62–64], $FeSn$ [65], and $Co_3Sn_2S_2$ [16], where the moment-bearing transition metals form a kagome lattice. Recently AV_3Sb_5 ($A = K, Rb, Cs$) systems have shown a charge density wave (CDW), superconductivity, and the anomalous Hall effect [66–68] all of which have opened up a new direction for exploring unconventional electronic properties associated with the nonmagnetic kagome layer. The V ions in RV_6Sn_6 possess no magnetic moment and form the kagome lattice. In particular, the kagome layer in these compounds contains no other atoms in the quasi-two-dimensional kagome network. Since RV_6Sn_6 ($R = Gd, Y, \text{ and } Sc$) compounds showed non-linear Hall resistivity, topologically nontrivial band structure, and CDW [22,23,69], it is of great interest to check other rare-earth-based compounds ($R = Tb - Tm$ and Lu) to see whether the unconventional electronic states exist in the whole family of materials. Note that we have become aware of recent publications that show similar results [70–72].

IV. SUMMARY

Single crystals of RV_6Sn_6 ($R = Y, Gd - Tm, Lu$) are grown by Sn flux and their physical properties are investigated by magnetization, specific heat, and resistivity measurements. Powder x-ray diffraction patterns reveal that these compounds crystallize into the $HfFe_6Ge_6$ -type structure, where V ions form a well-isolated kagome layer and rare-earth ions occupy a well-separated triangular lattice. Due to the CEF effects on rare-earth ions the magnetization as a function of temperature and magnetic field shows a large magnetic anisotropy, where the easy magnetization direction is the c axis for $R = Tb - Ho$ and ab plane for $R = Er$ and Tm . At low temperatures, the antiferromagnetic ordering is observed below 5 K for $R = Gd - Ho$ and no magnetic ordering is observed down to 1.8 K for $R = Er$ and Tm . Since V ions possess no magnetic moments, the magnetic properties of intermetallic RV_6Sn_6 compounds are solely governed by localized $4f$ electron moments.

ACKNOWLEDGMENTS

This work was supported by the Canada Research Chairs, Natural Sciences and Engineering Research Council of Canada, and Canada Foundation for Innovation program.

- [1] B. C. El Idrissi, G. Venturini, and B. Malaman, *Mater. Res. Bull.* **26**, 1331 (1991).
- [2] G. Venturini, B. C. El Idrissi, and B. Malaman, *J. Magn. Magn. Mater.* **94**, 35 (1991).
- [3] G. Venturini, R. Welter, and B. Malaman, *J. Alloys Compd.* **185**, 99 (1992).

- [4] J. Brabers, V. Duijn, F. De Boer, and K. Buschow, *J. Alloys Compd.* **198**, 127 (1993).
- [5] J. H. Brabers, K. H. Buschow, and F. R. de Boer, *J. Alloys Compd.* **205**, 77 (1994).
- [6] J. Cadogan and D. Ryan, *J. Alloys Compd.* **326**, 166 (2001).
- [7] G. Venturini, *Z. Kristallogr. Cryst. Mater.* **221**, 511 (2006).

- [8] G. Venturini, H. Ihou-Mouko, C. Lefevre, S. Lidin, B. Malaman, T. Mazet, J. Tobola, and A. Verniere, *Chem. Met. Alloys* **1**, 24 (2008).
- [9] A. Weiland, L. J. Eddy, G. T. McCandless, H. Hodovanets, J. Paglione, and J. Y. Chan, *Cryst. Growth Des.* **20**, 6715 (2020).
- [10] K. Buschow, *Rep. Prog. Phys.* **40**, 1179 (1977).
- [11] B. Malaman, G. Venturini, R. Welter, J. Sanchez, P. Vulliet, and E. Ressouche, *J. Magn. Magn. Mater.* **202**, 519 (1999).
- [12] F. Mulder, R. Thiel, J. Brabers, F. De Boer, and K. Buschow, *J. Alloys Compd.* **198**, L1 (1993).
- [13] P. Schobinger-Papamantellos, J. Rodríguez-Carvajal, and K. Buschow, *J. Alloys Compd.* **274**, 83 (1998).
- [14] A. Szytuła, E. Wawrzyńska, and A. Zygmunt, *J. Alloys Compd.* **366**, L16 (2004).
- [15] L. Ye, M. Kang, J. Liu, F. Von Cube, C. R. Wicker, T. Suzuki, C. Jozwiak, A. Bostwick, E. Rotenberg, D. C. Bell, L. Fu, R. Comin, and J. G. Checkelsky, *Nature (London)* **555**, 638 (2018).
- [16] Q. Wang, Y. Xu, R. Lou, Z. Liu, M. Li, Y. Huang, D. Shen, H. Weng, S. Wang, and H. Lei, *Nat. Commun.* **9**, 3681 (2018).
- [17] J. Yin, W. Ma, T. A. Cochran, X. Xu, S. S. Zhang, H.-J. Tien, N. Shumiya, G. Cheng, K. Jiang, B. Lian, Z. Song, G. Chang, I. Belopolski, D. Multer, M. Litskevich, Z. Cheng, X. P. Yang, B. Swidler, H. Zhou, H. Lin *et al.*, *Nature (London)* **583**, 533 (2020).
- [18] Y. Ishii, H. Harima, Y. Okamoto, J.-I. Yamaura, and Z. Hiroi, *J. Phys. Soc. Jpn.* **82**, 023705 (2013).
- [19] N. J. Ghimire, R. L. Dally, L. Poudel, D. Jones, D. Michel, N. T. Magar, M. Bleuel, M. A. McGuire, J. Jiang, J. Mitchell, J. S. Jiang, J. F. Mitchell, J. W. Lynn, and I. I. Mazin, *Sci. Adv.* **6**, eabe2680 (2020).
- [20] W. Ma, X. Xu, J.-X. Yin, H. Yang, H. Zhou, Z.-J. Cheng, Y. Huang, Z. Qu, F. Wang, M. Z. Hasan, and S. Jia, *Phys. Rev. Lett.* **126**, 246602 (2021).
- [21] S. Peng, Y. Han, G. Pokharel, J. Shen, Z. Li, M. Hashimoto, D. Lu, B. R. Ortiz, Y. Luo, H. Li, M. Guo, B. Wang, S. Cui, Z. Sun, Z. Qiao, S. D. Wilson, and J. He, *Phys. Rev. Lett.* **127**, 266401 (2021).
- [22] H. Ishikawa, T. Yajima, M. Kawamura, H. Mitamura, and K. Kindo, *J. Phys. Soc. Jpn.* **90**, 124704 (2021).
- [23] G. Pokharel, S. M. L. Teicher, B. R. Ortiz, P. M. Sarte, G. Wu, S. Peng, J. He, R. Seshadri, and S. D. Wilson, *Phys. Rev. B* **104**, 235139 (2021).
- [24] L. Romaka, Y. Stadyk, V. Romaka, P. Demchenko, M. Stadyshyn, and M. Konyk, *J. Alloys Compd.* **509**, 8862 (2011).
- [25] P. C. Canfield and Z. Fisk, *Philos. Mag. B* **65**, 1117 (1992).
- [26] B. H. Toby and R. B. Von Dreele, *J. Appl. Crystallogr.* **46**, 544 (2013).
- [27] B. Hatt, J. Page, and V. Rivlin, *J. Low Temp. Phys.* **10**, 285 (1973).
- [28] M. Tian, J. Wang, J. Snyder, J. Kurtz, Y. Liu, P. Schiffer, T. E. Mallouk, and M. Chan, *Appl. Phys. Lett.* **83**, 1620 (2003).
- [29] A. S. Sefat, S. L. Bud'ko, and P. C. Canfield, *J. Magn. Magn. Mater.* **320**, 120 (2008).
- [30] K. Myers, S. L. Bud'ko, I. Fisher, Z. Islam, H. Kleinke, A. Lacerda, and P. Canfield, *J. Magn. Magn. Mater.* **205**, 27 (1999).
- [31] S. L. Bud'ko, Z. Islam, T. Wiener, I. Fisher, A. Lacerda, and P. Canfield, *J. Magn. Magn. Mater.* **205**, 53 (1999).
- [32] M. Reehuis, A. Krimmel, N. Büttgen, A. Loidl, and A. Prokofev, *Eur. Phys. J. B* **35**, 311 (2003).
- [33] H. Kadowaki, K. Ubukoshi, K. Hirakawa, J. L. Martínez, and G. Shirane, *J. Phys. Soc. Jpn.* **56**, 4027 (1987).
- [34] W. H. Blades, A. C. Reber, S. N. Khanna, L. López-Sosa, P. Calaminici, and A. M. Köster, *J. Phys. Chem. A* **121**, 2990 (2017).
- [35] P. De Gennes, *J. Phys. Radium* **23**, 510 (1962).
- [36] D. Noakes and G. Shenoy, *Phys. Lett. A* **91**, 35 (1982).
- [37] E. Morosan, S. L. Bud'ko, and P. C. Canfield, *Phys. Rev. B* **72**, 014425 (2005).
- [38] M. Falkowski, B. Andrzejewski, and A. Kowalczyk, *J. Alloys Compd.* **442**, 155 (2007).
- [39] A. Szytuła, S. Baran, Ł. Gondek, A. Arulraj, B. Penc, and N. Stüsser, *Acta Phys. Pol. A* **117**, 590 (2010).
- [40] A. Marcinkova, C. de la Cruz, J. Yip, L. L. Zhao, J. K. Wang, E. Svanidze, and E. Morosan, *J. Magn. Magn. Mater.* **384**, 192 (2015).
- [41] N. Van Hieu, T. Takeuchi, H. Shishido, C. Tonohiro, T. Yamada, H. Nakashima, K. Sugiyama, R. Settai, T. D. Matsuda, Y. Haga, M. Hagiwara, K. Kindo, S. Araki, Y. Nozue, and Y. Onuki, *J. Phys. Soc. Jpn.* **76**, 064702 (2007).
- [42] L. Qian, S. Lei, B. K. Rai, C.-L. Huang, A. M. Hallas, G. T. McCandless, J. Y. Chan, and E. Morosan, *Phys. Rev. Materials* **5**, 094416 (2021).
- [43] Y. Wang, *Phys. Lett. A* **35**, 383 (1971).
- [44] P. Boutron, *Phys. Rev. B* **7**, 3226 (1973).
- [45] H. Zhou, S. Lambert, M. Maple, and B. Dunlap, *Philos. Mag.* **89**, 1861 (2009).
- [46] D. A. Huse and V. Elser, *Phys. Rev. Lett.* **60**, 2531 (1988).
- [47] T. Jolicoeur and J. C. Le Guillou, *Phys. Rev. B* **40**, 2727 (1989).
- [48] B. Bernu, P. Lecheminant, C. Lhuillier, and L. Pierre, *Phys. Rev. B* **50**, 10048 (1994).
- [49] R. R. P. Singh and D. A. Huse, *Phys. Rev. Lett.* **68**, 1766 (1992).
- [50] S. R. White and A. L. Chernyshev, *Phys. Rev. Lett.* **99**, 127004 (2007).
- [51] P. Fazekas and P. Anderson, *Philos. Mag.* **30**, 423 (1974).
- [52] D. Yamamoto, G. Marmorini, and I. Danshita, *Phys. Rev. Lett.* **112**, 127203 (2014).
- [53] B. Schmidt and P. Thalmeier, *Phys. Rev. B* **89**, 184402 (2014).
- [54] Y.-D. Li, X. Wang, and G. Chen, *Phys. Rev. B* **94**, 035107 (2016).
- [55] W. Witczak-Krempa, G. Chen, Y. B. Kim, and L. Balents, *Annu. Rev. Condens. Matter Phys.* **5**, 57 (2014).
- [56] H. Nakamura, N. Kim, M. Shiga, R. Kmieć, K. Tomala, E. Ressouche, J. P. Sanchez, and B. Malaman, *J. Phys.: Condens. Matter* **11**, 1095 (1999).
- [57] S. A. M. Mentink, A. Drost, G. J. Nieuwenhuys, E. Frikkee, A. A. Menovsky, and J. A. Mydosh, *Phys. Rev. Lett.* **73**, 1031 (1994).
- [58] O. Stockert, J.-U. Hoffmann, M. Mühlbauer, A. Senyshyn, M. M. Koza, A. A. Tsirlin, F. M. Wolf, S. Bachus, P. Gegenwart, R. Movshovich, S. Bobev, and V. Fritsch, *Phys. Rev. Research* **2**, 013183 (2020).
- [59] T. Kurumaji, T. Nakajima, M. Hirschberger, A. Kikkawa, Y. Yamasaki, H. Sagayama, H. Nakao, Y. Taguchi, T. Arima, and Y. Tokura, *Science* **365**, 914 (2019).
- [60] H. Zhang, Q. Huang, L. Hao, J. Yang, K. Noordhoek, S. Pandey, H. Zhou, and J. Liu, *New J. Phys.* **22**, 083056 (2020).
- [61] Y. Tokura and N. Kanazawa, *Chem. Rev.* **121**, 2857 (2021).
- [62] L. Fenner, A. Dee, and A. Wills, *J. Phys.: Condens. Matter* **21**, 452202 (2009).

- [63] T. Kida, L. Fenner, A. Dee, I. Terasaki, M. Hagiwara, and A. Wills, *J. Phys.: Condens. Matter* **23**, 112205 (2011).
- [64] H. Li, B. Ding, J. Chen, Z. Li, Z. Hou, E. Liu, H. Zhang, X. Xi, G. Wu, and W. Wang, *Appl. Phys. Lett.* **114**, 192408 (2019).
- [65] M. Kang, L. Ye, S. Fang, J.-S. You, A. Levitan, M. Han, J. I. Facio, C. Jozwiak, A. Bostwick, E. Rotenberg, M. K. Chan, R. D. McDonald, D. Graf, K. Kaznatcheev, E. Vescovo, D. C. Bell, E. Kaxiras, J. van den Brink, M. Richter, M. P. Ghimire, J. G. Checkelsky *et al.*, *Nat. Mater.* **19**, 163 (2020).
- [66] B. R. Ortiz, S. M. L. Teicher, Y. Hu, J. L. Zuo, P. M. Sarte, E. C. Schueller, A. M. Milinda Abeykoon, M. J. Krogstad, S. Rosenkranz, R. Osborn, R. Seshadri, L. Balents, J. He, and S. D. Wilson, *Phys. Rev. Lett.* **125**, 247002 (2020).
- [67] B. R. Ortiz, P. M. Sarte, E. M. Kenney, M. J. Graf, S. M. L. Teicher, R. Seshadri, and S. D. Wilson, *Phys. Rev. Materials* **5**, 034801 (2021).
- [68] Q. Yin, Z. Tu, C. Gong, Y. Fu, S. Yan, and H. Lei, *Chin. Phys. Lett.* **38**, 037403 (2021).
- [69] H. W. S. Arachchige, W. R. Meier, M. Marshall, T. Matsuoka, R. Xue, M. A. McGuire, R. P. Hermann, H. Cao, and D. Mandrus, [arXiv:2205.04582](https://arxiv.org/abs/2205.04582).
- [70] G. Pokharel, B. Ortiz, P. Sarte, L. Kautzsch, G. Wu, J. Ruff, and S. D. Wilson, [arXiv:2205.15559](https://arxiv.org/abs/2205.15559).
- [71] X. X. Zhang, Z. Y. Liu, Q. Cui, N. N. Wang, L. F. Shi, H. Zhang, X. L. Dong, J. P. Sun, Z. L. Dun, and J. G. Cheng, [arXiv:2206.05653](https://arxiv.org/abs/2206.05653).
- [72] E. Rosenberg, J. M. DeStefano, Y. Guo, J. S. Oh, M. Hashimoto, D. Lu, R. J. Birgeneau, Y. Lee, L. Ke, M. Yi, and J. Chu, [arXiv:2205.14802](https://arxiv.org/abs/2205.14802).